Controlled Quantum Operations of a Semiconductor Three-Qubit System

Hai-Ou Li,[1,3] Gang Cao,[1,3] Guo-Dong Yu,[2,3] Ming Xiao,[2,3,*] Guang-Can Guo,[1,3] Hong-Wen Jiang,[4] and Guo-Ping Guo[1,3,†]

[1]*Key Laboratory of Quantum Information, CAS, University of Science and Technology of China, Hefei, Anhui 230026, China*

[2]*Department of Optics and Optical Engineering, University of Science and Technology of China, Hefei, Anhui 230026, China*

[3]*Synergetic Innovation Center of Quantum Information & Quantum Physics, University of Science and Technology of China, Hefei, Anhui 230026, China*

[4]*Department of Physics and Astronomy, University of California, Los Angeles, California 90095, USA*

(Received 25 October 2016; revised manuscript received 7 December 2017; published 15 February 2018)

In a specially designed semiconductor device consisting of three capacitively coupled double quantum dots, we achieve strong and tunable coupling between a target qubit and two control qubits. We demonstrate how to completely switch on and off the target qubit's coherent rotations by presetting two control qubits' states. A Toffoli gate is, therefore, possible based on these control effects. This research paves a way for realizing full quantum-logic operations in semiconductor multiqubit systems.

DOI: 10.1103/PhysRevApplied.9.024015

I. INTRODUCTION

Qubits based on semiconductor quantum dots have made considerable progress in recent years. Single-electron spin qubits [1–6], single-charge qubits [7–10], or single-spin-charge hybrid qubits [11,12] have been demonstrated in both GaAs and silicon devices. Strongly coupled two qubits have also been realized in either spin [13–16] or charge [17,18] qubit systems.

The potential of scaling-up these electrically defined and manipulated devices is believed to be a major advantage of semiconductor qubits. A linear array of semiconductor quantum dots, for instance, has been utilized to study a series of interacting quantum systems [19,20]. However, it is still extremely challenging to achieve gate operations beyond the two-qubit limit, which will be of great technical and scientific value. Quantum gates for more than two qubits, such as a three-qubit Toffoli gate [21], will make quantum computation more effective and, hence, relieve the requirement of quantum error correction when performing multistep quantum-logic operations. It has also been predicted that three or more coupled qubits will be important to study quantum correlations among electrons, such as Greenberger-Horne-Zeilinger (GHZ) states [22,23].

Here we demonstrate a three-qubit system in a semiconductor quantum-dot device, combining the architectures of a linear array and a T-shaped triple-dot array (referred to as a T gate) to achieve effective control of coupling between a target qubit and two control qubits. The strong coupling allows us to control the energy spectroscopy of the target qubit by the states of two control qubits. Because of the coupling-induced detuning away from the energy resonance condition, we show experimentally that the target qubit's quantum rotations, including both amplitude and phase rotations, can be switched on and off nearly completely by setting the two control qubits to certain eigenstates. The functionalities of a Toffoli gate are, therefore, demonstrated. At the end of the paper, we also analyze the technical challenges needed to overcome in order to implement full quantum three-qubit gates.

II. SYSTEM AND THEORY

A. Strong and tunable interqubit couplings

Our devices are defined via electron-beam lithography on a GaAs/(Al30%, Ga70%)As heterostructure. Figure 1(a) is a scanning electron microscopy (SEM) image of a typical device. On the top, the first (second) double quantum dot (DQD) is defined by gates H_L, H_R, and $U_1 - U_5$ ($U_5 - U_9$). On the bottom, the third DQD is defined by gates H_L, H_R, and $L_1 - L_5$. Three quantum-point contacts (QPCs) defined by gates Q_1, Q_2, and Q_3 detect the location of a valance electron on each DQD. Standard lock-in modulation and detection techniques are used for charge sensing [24]. The experiments are performed in an Oxford Triton dilution refrigerator with a base temperature of 10 mK. Each DQD behaves as a charge qubit. The Hamiltonian of this three-qubit system is

*Corresponding author.
maaxiao@ustc.edu.cn
†Corresponding author.
gpguo@ustc.edu.cn

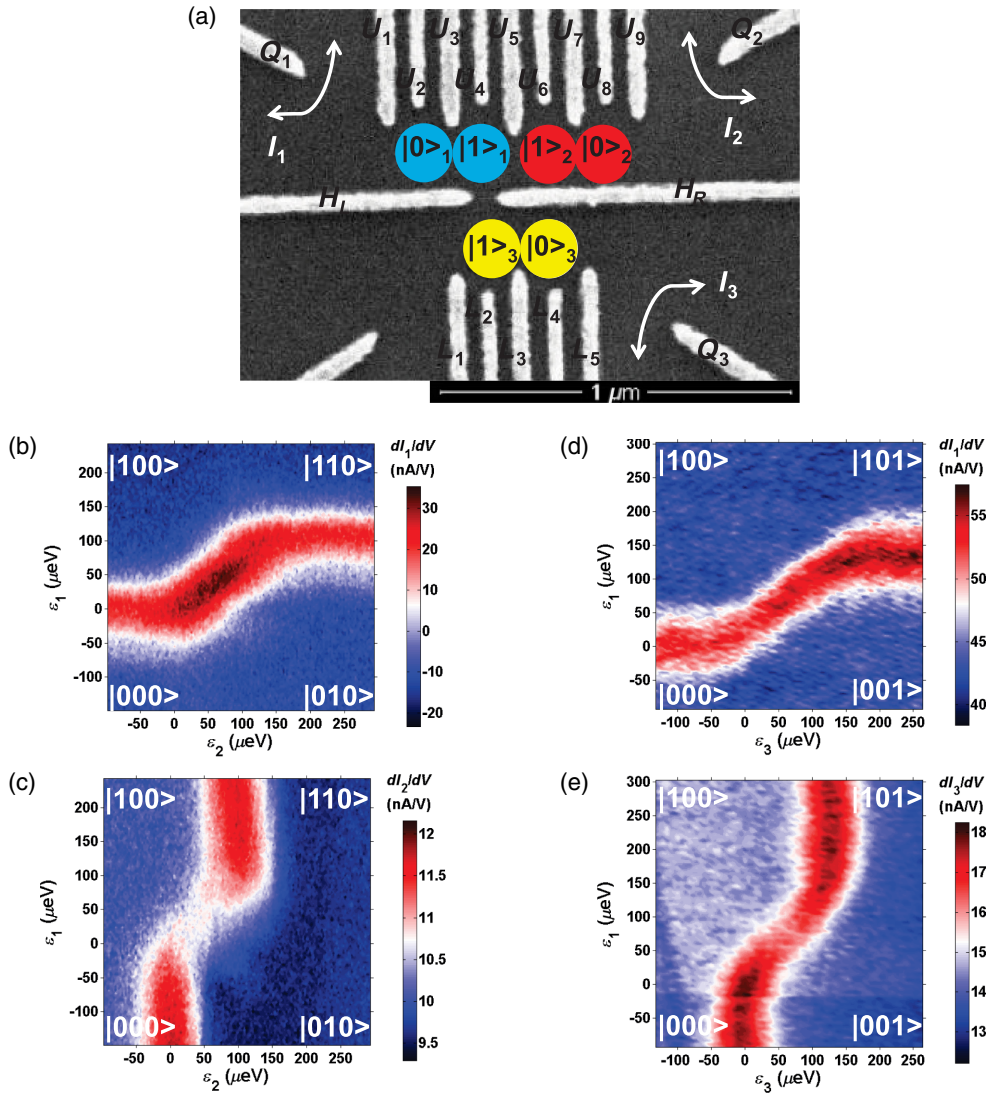

FIG. 1. (a) SEM image of three coupled qubits. (b),(c) Coupling energy J_{12} between qubit 1 and qubit 2. Qubit 3 is fixed at $|0\rangle_3$. Presented are differential currents measured by QPC 1 and QPC 2, respectively. (d),(e) Coupling energy J_{13} between qubit 1 and qubit 3. Qubit 2 is fixed at $|0\rangle_2$. Presented are differential currents measured by QPC 1 and QPC 3, respectively.

$$H_{3q} = H_1 \otimes I \otimes I + I \otimes H_2 \otimes I + I \otimes I \otimes H_3 + J_{12}\frac{I-\sigma_z}{2} \otimes \frac{I-\sigma_z}{2} \otimes I + J_{13}\frac{I-\sigma_z}{2} \otimes I \otimes \frac{I-\sigma_z}{2}. \quad (1)$$

Here, $H_i = (\varepsilon_i\sigma_z + \Delta_i\sigma_x)/2$ is the Hamiltonian of the ith qubit, with ε_i and $\Delta_i/2$ being its energy detuning and interdot tunneling rate, respectively. σ_x and σ_z are the Pauli matrixes, and I is the identity matrix. J_{12} (J_{13}) is the coupling energy between qubit 1 and qubit 2 (qubit 3). We describe the qubit evolution in the framework of the eigenstates of H_{3q}: $|000\rangle$, $|100\rangle$, $|010\rangle$, $|110\rangle$, $|001\rangle$, $|101\rangle$, $|011\rangle$, and $|111\rangle$. The definitions of $|0\rangle$ and $|1\rangle$ for each qubit are indicated in Fig. 1(a), where $|0>_1 |0>_2 |0>_3$ corresponds to $|000\rangle$ and so on. For consistency, we define $|0\rangle$'s ($|1\rangle$'s) as the states where the neighboring qubits are far apart (closely located).

We set qubit 1 as the target qubit and the other two as the control qubits. We demonstrate that it is feasible to control quantum operations of the target qubit by the states of the two control qubits due to their strong coupling. When the electron in the target qubit is far from the two electrons in both control qubits corresponding to state $|000\rangle$, their coupling energy is smallest and we denote it as zero. When the target electron is close to the second (third) electron and far from the third (second) electron corresponding to state $|110\rangle$ ($|101\rangle$), their coupling energy is J_{12} (J_{13}). In state $|111\rangle$, the largest coupling energy $J_{12} + J_{13}$ arises because the target electron is close to both control electrons.

In Figs. 1(b)–1(e), we present the experimentally measured coupling energies. In Figs. 1(b) and 1(c), we sweep ε_1 against ε_2 while fixing qubit 3 at state $|0\rangle_3$ ($\varepsilon_3 \ll 0$) and measure the differential current of QPC 1 and QPC 2. The detunings are converted through the voltage on relative plunger gates. For instance, to increase ε_1, we decrease V_{U2} and simultaneously increase V_{U4}. The energy-conversion factor for this gate compensation scanning can be obtained through photon-assisted tunneling (PAT). In this experiment, the conversion

factors for three qubits are from 32 to 38 μeV/mV [25,26]. We see an abrupt shift in each QPC signal around the anticrossing points ($\varepsilon_1 = \varepsilon_2 = 0$). As both ε_1 and ε_2 go from the negative side through the anticrossing point to the positive side, the three-qubit state changes from $|000\rangle$ to $|110\rangle$. Coupling energy J_{12} shifts the anticrossing point toward the positive side. The amount of this shift directly tells us that the value of J_{12} is about 105 μeV [25,27]. In Figs. 1(d) and 1(e), we fix qubit 2 at $|0\rangle_2$ and do the same measurement for qubit 1 and qubit 3. In the same way, the abrupt energy shift around the anticrossing points ($\varepsilon_1 = \varepsilon_3 = 0$) tells us that J_{13} is approximately 135 μeV.

The measured values of J_{12} and J_{13} are large in the following sense. J_{12} and J_{13} are much larger than Δ_1 (Δ_1 about 4.5 GHz or $h\Delta_1$ about 18 μeV in this experiment), which is the scale of energy spacing at the target qubit's anticrossing point. When the target qubit is coupled to either control qubit, an energy shift by J_{12} or J_{13} away from the anticrossing point is, therefore, large with regard to Δ_1. We see in the later contexts from both experimental data and theoretical simulations that these large energy shifts enable us to effectively control the target qubit's coherent rotations. Finally, J_{12} and J_{13} are comparable with the interqubit coupling energy in an earlier two-qubit system, where the large coupling enables us to perform a controlled-NOT logic gate [18].

To achieve strong multiple qubit coupling, we use both linear-array and T-gate architectures, which give rise to J_{12} and J_{13}, respectively. The linear-array architecture has the flexibility to couple more numbers of qubits. However, it seems that T-gate architecture is more effective in tuning interqubit coupling. The gap distance between H_L and H_R is very narrow (<80 nm), and this allows us to tune J_{13} into a strong regime while forbidding direct tunneling [18,27]. J_{13} can be repeatedly tuned from 0 to above 100 μeV without any detectable tunnel coupling. Qubit 1 and qubit 2 are closely neighbored. Their coupling strength could also be very strong. However, if their commonly shared gate U_5 is not sufficiently closed, tunneling usually happens, and capacitive coupling quickly decreases if U_5 is closed too much. Therefore, the linear array device seems to have a narrow window to achieve strong capacitive coupling without tunneling. In the experiment, we have to deliberately tune U_5, H_L, and H_R for this purpose [28].

The coupling between qubit 2 and qubit 3 is screened by gate H_R and is normally measured to be less than one-fifth of J_{13}. Therefore, this coupling is neglected in our consideration. Many interesting three-qubit operations can still be realized using this geometry. For instance, principally, the three qubits can be set into a GHZ state by coupling qubit 1 and the other two qubits, without a coupling between qubit 2 and qubit 3 [23].

B. Mechanism of controlled coherent rotations

These large coupling strengths enable us to implement three-qubit operations [18,29]. The coherent rotations of the target qubit, such as Larmor precession [8], Landau-Zener-Stückelberg (LZS) interferences [9], and Rabi oscillations [10], usually occur when the qubit is brought from an initial state to its anticrossing point. Now we take the example of Larmor precession to illustrate the mechanism of controlled coherent rotations: we initialize the target qubit at $|0\rangle_1$ and apply a nonadiabatic voltage pulse to drive it to its anticrossing point, where coherent rotations between $|0\rangle_1$ and $|1\rangle_1$ occur. In fact, the same mechanism applies to LZS interferences if an adiabatic passage drives the target qubit across its anticrossing point and to Rabi oscillations if a microwave pulse is shined whose frequency meets the resonance condition at the anticrossing point.

In Fig. 2(a), we calculate three-qubit energy spectroscopy as a function of ε_1 while fixing the control qubits at $|0\rangle_2|0\rangle_3$ ($\varepsilon_2 = \varepsilon_3 = -200$ μeV). The experimental values of J_{12} and J_{13} are used. Particularly, we are interested in the ground state and the first excited state of the target qubit. In the working energy range, say, -200 μeV $< \varepsilon_1 <$ 200 μeV, the two lowest energy states are $|000\rangle$ and $|100\rangle$ shown as the blue solid and dashed lines. Their anticrossing point is at $\varepsilon_1 = 0$. If we initialize $\varepsilon_1 \ll 0$ and pulse ε_1 to 0, coherent rotations between $|000\rangle$ and $|100\rangle$ will occur.

In Figs. 2(b)–2(d), we simulate the change of energy spectroscopy for different states of control qubits. Only the few relevant lowest energy levels are depicted. In Fig. 2(b), ε_2 and ε_3 are set as 200 and -200 μeV, respectively. We see that the anticrossing point between the two lowest target qubit states $|010\rangle$ and $|110\rangle$ shifts to $\varepsilon_1 = J_{12} = 105$ μeV. Consequently, if we still initialize $\varepsilon_1 \ll 0$ and pulse ε_1 to 0, the target qubit falls below its anticrossing point by 105 μeV. It is such a huge amount that the coherent rotations will be nearly completely suppressed. After the pulse finishes, the qubits simply return to initial state $|010\rangle$. In Fig. 2(c), ε_2 and ε_3 are set as -200 and 200 μeV, respectively. The anticrossing point between $|001\rangle$ and $|101\rangle$ shifts to $\varepsilon_1 = J_{13} = 135$ μeV. Finally, ε_2 and ε_3 are both set as 200 μeV in Fig. 2(d). The anticrossing point between $|011\rangle$ and $|111\rangle$ shifts to $\varepsilon_1 = J_{12} + J_{13} =$ 240 μeV. In all three cases, the pulse cannot drive the target qubit to its anticrossing point, and the coherent rotations will be greatly suppressed.

The suppression of coherent oscillations is because of the fact that the rotation amplitude of Larmor precession, LZS interferences, and Rabi oscillations reaches the maximum at the anticrossing point and deteriorates quickly with respect to the detuning for this two-level quantum system. In addition, the qubit coherence time also reaches the maximum at the anticrossing point [8]. The enhanced decoherence away from the anticrossing point will definitely help suppress the coherent oscillations. However, we think it does not play a major role here.

The coherence effect happens symmetrically on both sides around the anticrossing point. The experimentally observed Larmor oscillations, on the contrary, are asymmetric due to

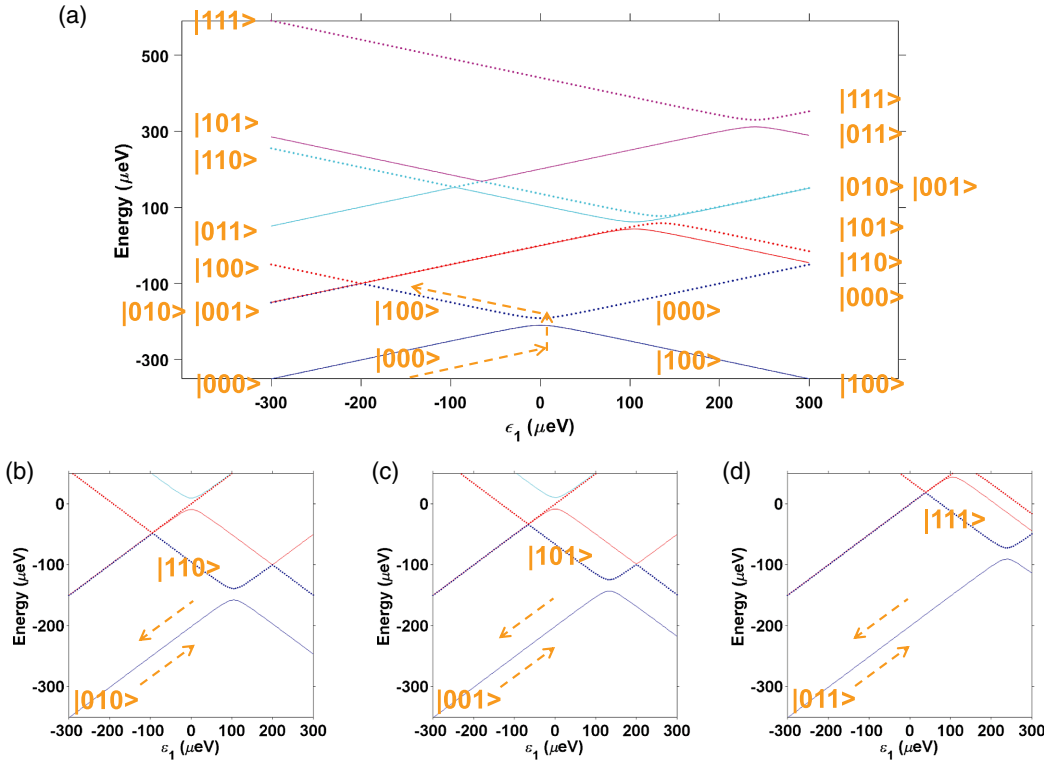

FIG. 2. (a) Simulated three-qubit energy spectroscopy. The detuning of qubit 2 and qubit 3 is fixed far below the anticrossing points so that their ground state is $|0\rangle_2|0\rangle_3$. (b)–(d) Qubit 2 and qubit 3 are configured so that their ground states are $|1\rangle_2|0\rangle_3$, $|0\rangle_2|1\rangle_3$, and $|1\rangle_2|1\rangle_3$, respectively. Only the few relevant lowest levels are shown.

the adiabaticity of the operation pulse. The Larmor oscillations have a limited line width below the anticrossing point and have a much broader decaying tail above this point [28]. If we intentionally increase the amplitude of the operation pulse to drive the qubit above the anticrossing point by a same amount as J, we see decayed Larmor oscillations with residual amplitude, which is due to the decoherence effect. The decoherence effect alone requires a much larger energy shift than J to completely suppress the Larmor oscillations. On the other hand, in our control experiment, when the target qubit is coupled to the control qubits, its energy levels elevate, and the operation pulse falls below its anticrossing point. The Larmor oscillations are then completely suppressed since the J-induced energy shift is already larger than its line width. In conclusion, it is mainly the coupling-induced detuning away from the resonance condition that completely suppresses the coherent oscillations.

III. RESULTS AND DISCUSSION

A. Controlled amplitude rotations and Toffoli gate

Now we introduce our experimental results. We initialize the qubits at state $|000\rangle$ and apply a nonadiabatic rectangular voltage pulse to the target qubit to drive the qubits exactly to the anticrossing point between $|000\rangle$ and $|100\rangle$. Larmor precession occurs. The target qubit rotates between $|0\rangle_1$ and $|1\rangle_1$ by an angle $2\pi\Delta_1 W_1$, where W_1 is the pulse width. This Larmor procession allows us to coherently manipulate the amplitude of the target qubit's wave function. Then we vary the initial state to $|010\rangle$, $|001\rangle$, or $|011\rangle$ to suppress the coherent rotations of the target qubit, as we explain above.

In Fig. 3(a), we fix qubit 2 in $|0\rangle_2$ and control the amplitude rotations of qubit 1 by qubit 3. Clearly, coherent oscillations are observed when qubit 3 is in $|0\rangle_3$ ($\varepsilon_3 \ll 0$). These oscillations are Larmor procession of qubit 1, with a frequency $\Delta_1 = 4.5$ GHz consistent with the value obtained from PAT measurements [30]. On the other hand, when qubit 3 is in $|1\rangle_3$ ($\varepsilon_3 \gg 0$), the coherent rotations are gone.

Similarly, in Fig. 3(b), we fix qubit 3 in $|0\rangle_3$ and show the control effect of qubit 2. Larmor oscillations are observed when qubit 2 is in $|0\rangle_2$ and are suppressed when qubit 2 switches to $|1\rangle_2$. We see that both control qubits can effectively turn on and turn off the target qubit's coherent rotations.

In Fig. 3(c), we give a simulation to this control effect by numerically solving the Liouville–von Neumann equation regarding Hamiltonian H_{3q}. We use experimental parameters including decoherence time $T_2^* = 1.2$ ns [18,24]. Qubit 3's control effect on qubit 1 is shown. Qubit 2's control effect is similar. The simulation agrees with the experimental results.

Based on these control effects, we explore the basic functionality of a Tofolli gate. In Fig. 3(d), we sweep W_1 and vary the states of two control qubits covering all four eigenstates: $|0\rangle_2|0\rangle_3$, $|0\rangle_2|1\rangle_3$, $|1\rangle_2|0\rangle_3$, and $|1\rangle_2|1\rangle_3$. The black curve shows typical Larmor oscillations when the control qubits are in $|0\rangle_2|0\rangle_3$, while the other three curves show just background variations when the control qubits are in states $|0\rangle_2|1\rangle_3$, $|1\rangle_2|0\rangle_3$, or $|1\rangle_2|1\rangle_3$. These results

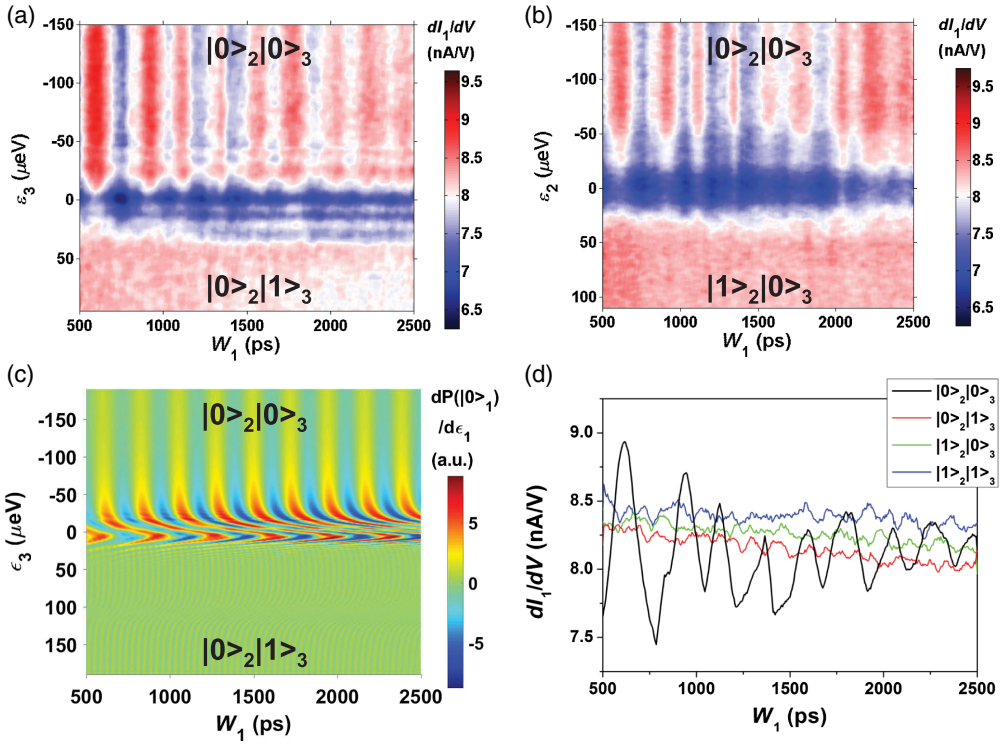

FIG. 3. (a),(b) Coherent amplitude rotations of qubit 1 controlled by qubit 3 and qubit 2, respectively. (c) Theoretical simulation of (a). Presented is the $|0\rangle_1$-state probability differentiated over ε_1. (d) Qubit 1's coherent rotations controlled by two control qubits all together. Qubit 2 and qubit 3 are set as $|0\rangle_2|0\rangle_3$, $|0\rangle_2|1\rangle_3$, $|1\rangle_2|0\rangle_3$, and $|1\rangle_2|1\rangle_3$, respectively.

indicate that a Toffoli gate is possible if we fix W_1 at about 615 ps: qubit 1's amplitude will reverse if both control qubits are in state $|0\rangle$ and will remain unchanged if any control qubit is in state $|1\rangle$.

B. Controlled phase rotations

Apart from controlling the target qubit's amplitude rotations, we can also control its phase rotations. As we noticed earlier [9], when we apply an ultrashort voltage pulse (100 to 350 ps in width), the transmission line acts as a low-pass filter and effectively modifies the pulse into Gaussian-like shape. Consequently, we observe LZS interferences as the pulse drives the qubit to its anticrossing point where a nonadiabatic transition occurs. This nonadiabatic transition corresponds to a rotation of the wave function's amplitude. Meanwhile, following the Gaussian pulse, adiabatic evolutions along two energy levels give rise to phase rotations. The frequency of the amplitude rotations is $\Delta_1 = 4.5$ GHz. The phase-rotation frequency is determined by both the height and width of the Gaussian pulse and can be tuned much faster than Δ_1 [9]. In this experiment, it reaches about 15 GHz. Therefore, we mainly focus on the fast phase rotations.

Figures 4(a) and 4(b) show the experimental data. First, we initialize the qubits at state $|000\rangle$. We apply to the target qubit an ultrashort voltage pulse. We choose the pulse height such that it drives the target qubit across its anticrossing point and induces LZS interferences. Next, we change the initial state to $|010\rangle$, $|001\rangle$, or $|011\rangle$, under which circumstances the same pulse is unable to drive the target qubit above its anticrossing point and phase rotations cease.

Qubit 2 is set at $|0\rangle_2$ in Fig. 4(a) and at $|1\rangle_2$ in Fig. 4(b). We change qubit 3 from $|0\rangle_3$ to $|1\rangle_3$ by scanning ε_3. Therefore, we are comparing the phase rotations of the target qubit for all four configurations of control qubits: $|0\rangle_2|0\rangle_3$, $|0\rangle_2|1\rangle_3$, $|1\rangle_2|0\rangle_3$, and $|1\rangle_2|1\rangle_3$. For $|0\rangle_2|0\rangle_3$, Fig. 4(a) shows persistent fast rotations. Roughly, we can see that a 2π phase rotation costs about 65 ps (15 GHz).

For configurations $|0\rangle_2|1\rangle_3$ and $|1\rangle_2|0\rangle_3$, these fast and clear rotations are gone. There are some residual background fluctuations. These are due to the large pulse amplitude to drive the target qubit across, more than exactly to, its anticrossing point to induce LZS interferences. For configurations $|0\rangle_2|1\rangle_3$ and $|1\rangle_2|0\rangle_3$, this large pulse may reach close to the anticrossing point and, therefore, causes residual oscillations. Nonetheless, both experiments and simulations show that these residual oscillations are very weak compared with the rotations in the $|0\rangle_2|0\rangle_3$ configuration. Furthermore, increasing the coupling strengths will completely eliminate these residuals. For $|1\rangle_2|1\rangle_3$, the coupling energy nearly doubles those of the former two configurations. In this case, the residual fluctuations disappear, meaning that the phase rotations are completely suppressed.

The above experiment shows that the target qubit's phase rotations can be turned on or off by varying two control qubits' states. Principally, a nonadiabatic pulse and an adiabatic pulse can be combined to make arbitrary quantum operations for a qubit, including both amplitude and phase rotations [31] and, therefore, to perform arbitrary three-qubit controlled quantum operations.

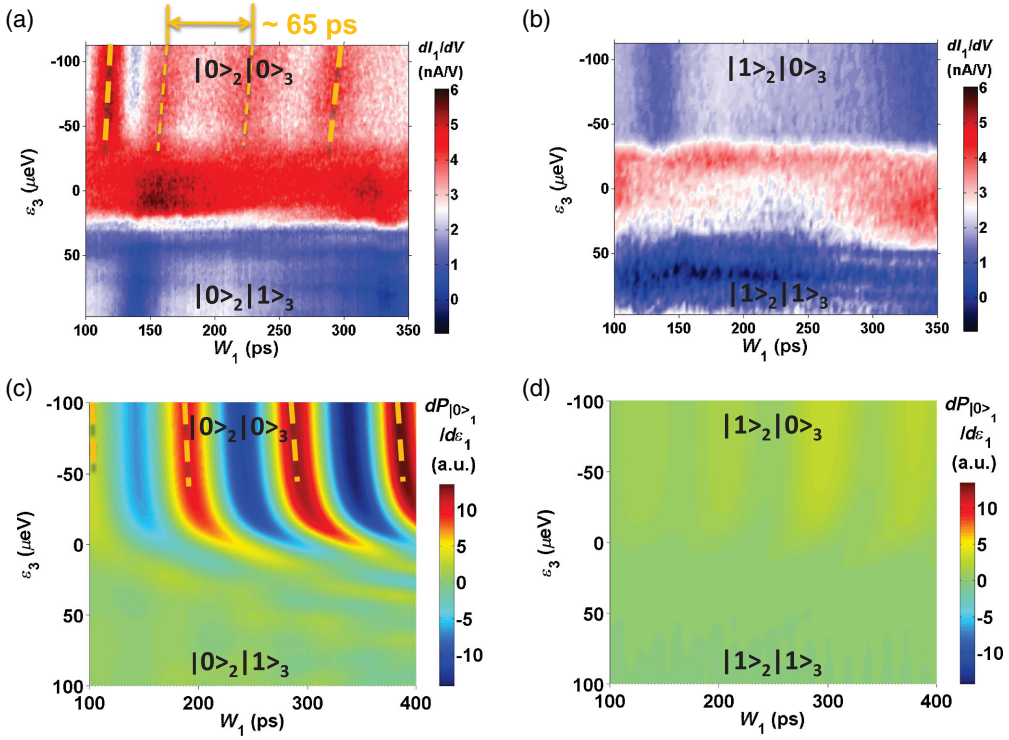

FIG. 4. (a),(b) Coherent phase rotations of qubit 1 controlled by qubit 2 and qubit 3, respectively. Qubit 2 is fixed at state $|0\rangle_2$ and $|1\rangle_2$, respectively. (c),(d) Theoretical simulations.

Figures 4(c) and 4(d) show our simulation results, which basically support the experimental data. We also notice some deviations. In Fig. 4(a), the observed phase rotations are not ideally periodic as predicated in Fig. 4(c). We think this indicates the existence of pulse reflection. The pulse may reflect back and forth. When the original pulse is ultrashort (<150 ps), the reflection pulse is superimposed on the peak of the original pulse and mainly increase its height. When the original pulse is wider (>150 ps), the reflection pulse is superimposed on the shoulder of the original pulse and mainly increases its width. Therefore, the LZS phase-rotation period becomes shorter when $W_1 <$ 150 ps because it decreases with pulse height and increases with pulse width [32]. This pulse imperfection is an example of the extreme technical challenges we face to implement full coherent three-qubit control, considering the requirement of precise synchronization and alignment of multiple ultrashort pulses.

IV. CONCLUSION

In summary, in a semiconductor three-qubit system, we demonstrate gate-voltage control of strong interqubit couplings by using a specially designed device structure. We successfully demonstrate coherent control of both amplitude and phase of one target qubit by the preprepared states of two control qubits and the basic functionalities of a Toffoli gate. We hope our first work in a semiconductor to go beyond the two-qubit limit will provide useful insight into research on multiple qubits in semiconductor devices. A natural extension of this work will be the dynamic control of all qubits to realize full quantum gates. Multiple ultrashort pulses need to be precisely synchronized to coherently rotate each qubit. Another equally important task is to improve the sensitivity of all QPCs to read out the probability of each qubit state.

ACKNOWLEDGMENTS

This work is supported by the National Key R&D Program (Grant No. 2016YFA0301700), the NSFC (Grants No. 11575172, No. 61674132, No. 11674300, No. 11625419, and No. 91421303), the SPRP of CAS (Grant No. XDB01030000), and the Fundamental Research Fund for the Central Universities. This work is partially carried out at the USTC Center for Micro and Nanoscale Research and Fabrication.

H.-O. L., G. C., and G.-D. Y contributed equally to this work.

APPENDIX A: QPC CHARGE SENSING

We use the modulation technique to increase the signal-noise ratio in charge occupation detection. Basically, we modulate a plunger gate of each quantum dot with the ac sine out of a lock-in amplifier and measure the ac component of each QPC current at the modulated frequency. The lock-in ac sine out is combined with a dc bias voltage before it is applied to the plunge gates. The QPC of each quantum dot is biased with dc current in the range of 1–2 nA. The ac voltage component on

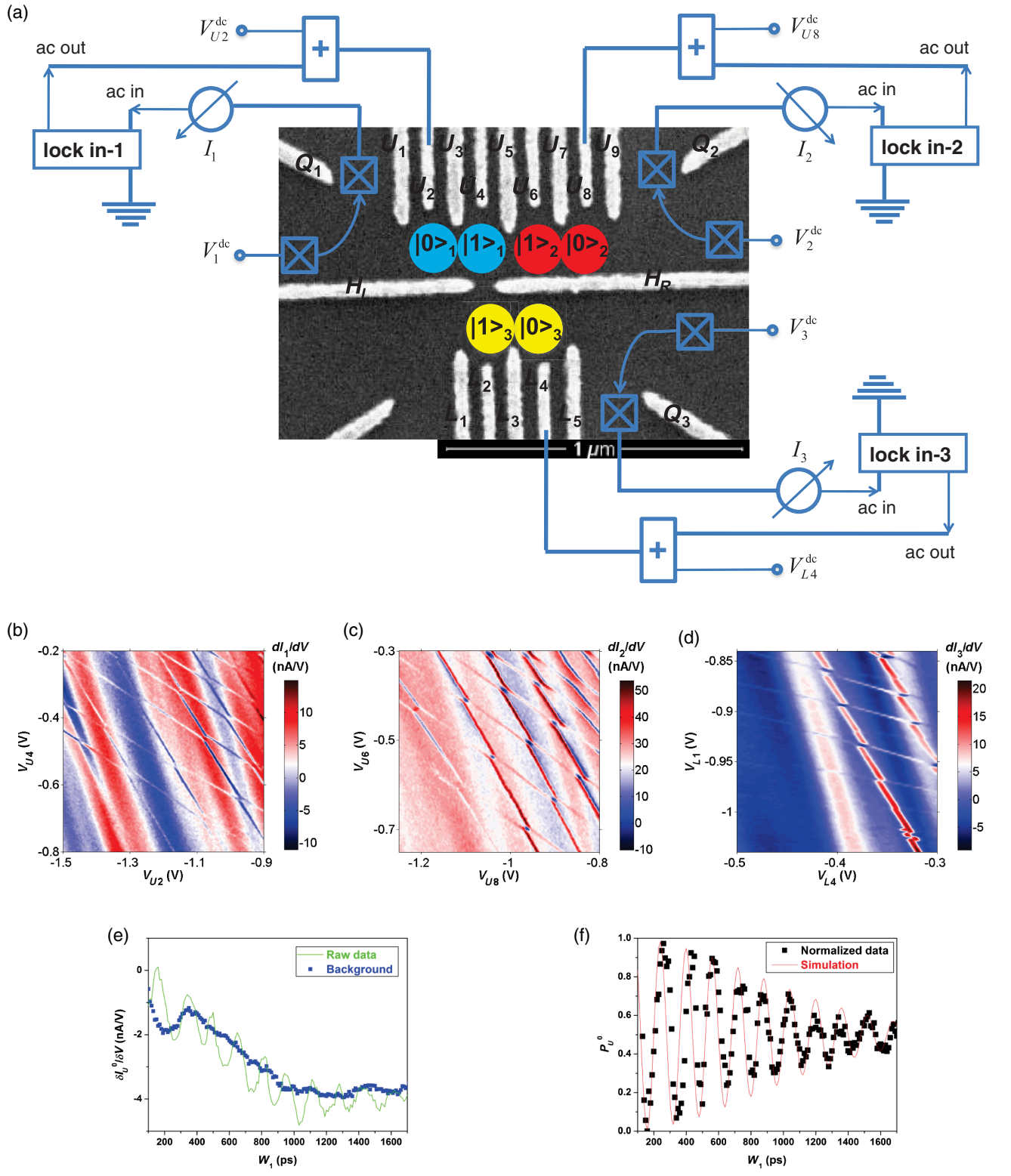

FIG. 5. (a) Sketch diagrams of the modulation measurement of all the three double quantum dots. (b)–(d) Charge stability diagrams of all three double quantum dots measured through the differential current of each QPC. (e) The green dotted line represents the raw data of the Larmor oscillations of qubit 1 detected by the transport current through the QPC formed by gates L_1, L_2, and L_3. The blue solid line represents the background curve. (f) The black dotted curve represents normalized Larmor oscillations obtained by dividing the raw data by the background. The red solid line represents the theoretical fit.

he plunger gate modulates the electron energy on the quantum dot, and the ac current component senses the resulted variation of electron charge occupation on the dot. Therefore, in this way, we are actually differentiating the QPC current with respect to the plunger gate voltage, or, equivalently, measuring the derivative of the charge occupation with respect to the electron energy.

This technique is proven to provide a better signal-to-noise ratio and is widely accepted in this research area. In Fig. 5(a), we illustrate the block diagrams for all three QPCs. Because we have three double quantum dots, we need to carefully choose the ac frequencies for each lock-in amplifier to avoid mutual interference. For instance, we can set the frequencies on each lock-in as 73, 173, and 231 Hz, respectively. In Figs. 5(b)–5(d), we show the measured charge diagrams for each quantum dot.

We can also detect the dc transport current through the QPCs to directly measure the probability of qubit states. However, because of the large number of qubits, the working ranges of the QPCs are limited, and the probability measurement cannot give results when all qubits are functioning. Nonetheless, we directly measure the probability of qubit states for a single qubit to calibrate the device. For instance, we can set voltages on L_1, L_2, and L_3 to form a single dot and to function as a sensitive QPC, which can be utilized to measure the probability of qubit 1's states. Figures 5(e) and 5(f) show an example of Larmor oscillations for qubit 1. Figure 5(e) records the transport current through the QPC formed by gates L_1, L_2, and L_3. After proper numerical processing, we obtain normalized qubit-state probability. The Larmor oscillations have a decaying envelope due to the dephasing time T_2^*, whose value is estimated to be around 1.2 ns by fitting the Larmor oscillations with a decaying cosine curve: $a_0 \exp[-(W_1/T_2^*)^2]\cos(2\pi\Delta_1 W_1 + b_0) + a_1 W_1 + a_2$.

APPENDIX B: CONVERT GATE VOLTAGES TO DETUNING ENERGY

In the main text, we always show the detuning energies for each qubit. Experimentally, these detunings are obtained in the following way. For example, Fig. 6 shows how we convert the voltages to detuning energies when measuring the coupling strength between qubit 1 and qubit 2. Figs. 6(a) and 6(b) present the charge stability diagrams of qubit 1 and qubit 2, respectively. Taking qubit 1 as an example, we increase V_{U2} and decrease V_{U4} simultaneously to vary the detuning energy ε_1 from negative to positive value. This is done along the blue dashed line shown in Fig. 6(a). Suppose voltages on gates $U2$ and $U4$ are changed by ΔV_{U2} and ΔV_{U4}, respectively, the detuning ε_1 can be described as [25]

$$\begin{aligned}\varepsilon_{1L} &= -\alpha_2 \Delta U_2 - k_4 \alpha_2 \Delta U_4,\\ \varepsilon_{1R} &= -\alpha_4 \Delta U_4 - k_2 \alpha_4 \Delta U_2,\\ \varepsilon_1 &= \varepsilon_{1L} - \varepsilon_{1R} = -(\alpha_2 - k_2\alpha_4)\Delta U_2\\ &\quad - (\alpha_4 - k_4\alpha_2)\Delta U_4.\end{aligned}$$

Here, α_2 and α_4 are the energy lever arms of V_{U2} and V_{U4}, respectively; $k_2 < 1$ and $k_4 < 1$ describe the cross talking between two gates. If the slope of the blue dashed line is $-tg(\theta)$, then $\Delta V_{U4} = -tg(\theta)\Delta V_{U2}$ and ε_1 can be estimated through the variation of V_{U2} alone:

$$\begin{aligned}\varepsilon_1 &= -\left[1 + tg(\theta)\frac{\alpha_4 - k_4\alpha_2}{\alpha_2 - k_2\alpha_4}\right](\alpha_2 - k_2\alpha_4)\Delta U_2\\ &\equiv -\gamma_2 \Delta U_2.\end{aligned}$$

The ideal case is to compensate ΔV_{U2} and ΔV_{U4} in such a way that the total energy $\varepsilon_{1L} + \varepsilon_{1R}$ remains unchanged. Based on this, we can calculate the ideal value of $tg(\theta)$. Practically, we choose $tg(\theta)$ close to the ideal value and try not to change it in the following experiments.

The lever arms α_i and k_i can be obtained from quantum-dot Coulomb blockade diamonds and charge stability diagrams. A more direct way to obtain the energy-conversion factor γ_i is through PAT measurement. Shining a microwave to one gate of qubit 1, in the proper conditions we see the PAT effect caused by electrons absorbing the energy of one or more photons and tunneling from one side of the DQD to the other side. We scan ΔV_{U2} and compensate ΔV_{U4} in the way that we describe above and measure the voltage spacing between the two observed PAT peaks (valleys). The relationship between the voltage spacing and the photon energy will tell us the energy conversion factor γ_2. Experimentally, we calculate that γ_2 is approximately 35 μeV/mV. For qubit 2, the conversion factor of ΔV_{U8} is about 38 μeV/mV. For qubit 3, the conversion factor of ΔV_{L4} is estimated to be 32 μeV/mV. These values are in the same magnitude as the lever arms α_2, α_4, and so on, as obtained in the quantum-dot transport measurement. More details of the PAT measurement can be found in our earlier papers [33,34].

Figures 6(c) and 6(d) present the measurement of coupling strength J_{12} when we vary V_{U2} and compensate V_{U4}, and vary V_{U8} and compensate V_{U6}, as indicated by the blue dashed lines in Figs. 6(a) and 6(b). After subtracting the offsets from and multiplying the conversion factors to the gate voltages, we convert the x axis and y axis into detuning energies, as shown in Figs. 6(e) and 6(f). From these two figures, we can tell that J_{12} is about 105 μeV.

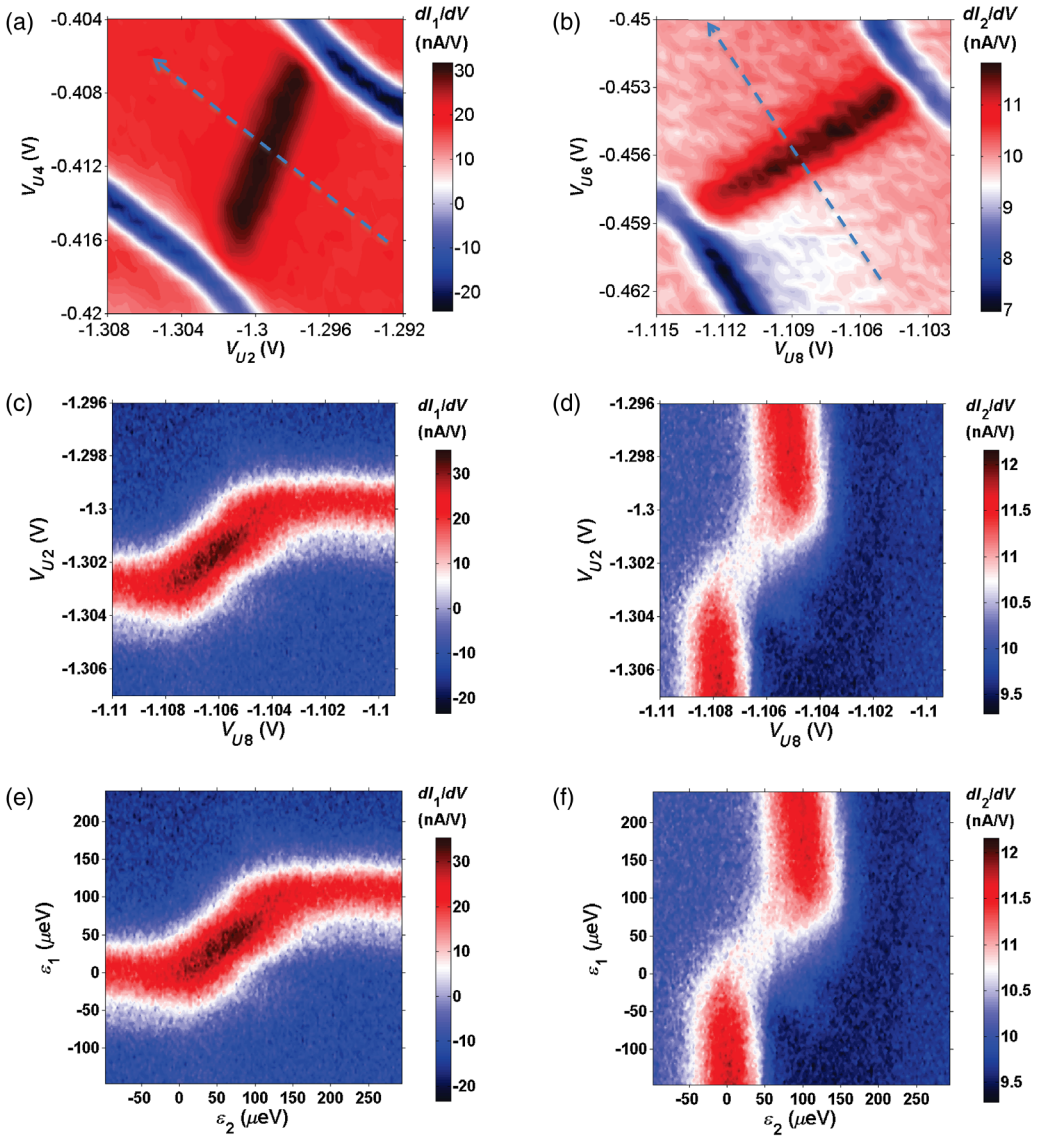

FIG. 6. (a),(b) Charging diagram of qubit 1 and qubit 2. Blue dashed lines indicate the direction of gate compensation and detuning energy variation. (c), (d) To measure the coupling energy J_{12}, we scan V_{U8} and compensate V_{U6} to vary ε_2, and scan V_{U4} and compensate V_{U2} to vary ε_1. (e), (f) Voltage values are converted to energy.

APPENDIX C: TUNING OF COUPLING ENERGY

Figures 7(a) and 7(b) show the measurement of J_{13} as we close gate voltage V_H to −0.85 V. The results tell us that J_{13} is about 50 μeV. This is much smaller than the one presented in Figs. 1(d) and 1(e), where J_{13} is about 135 μeV and V_H is much more open (−0.81 V). This means that adjusting the voltage on a pair of "T gates" ($H1$ and $H2$) can effectively tune the coupling between qubit 1 and qubit 3.

We try to repeat controlling the coherent rotations of qubit 1 by the state of qubit 3 when V_H is −0.85 V. The data are shown in Fig. 7(c). We can see that although the state of qubit 3 has an effect on the Larmor oscillations of qubit 1, there are obviously considerable residual oscillations when qubit 3 is switched to state $|1\rangle_3$. This partial suppression of Larmor oscillations suggests that in this condition, J_{13} is not strong enough, and the energy spectrum of qubit 1 does not shift far enough away after coupled to qubit 3.

In Fig. 7(d), we show that we can systematically tune the value of J_{13} by closing or opening V_H. These data are taken in another device with similar geometry and have been reported elsewhere [27]. The voltage value is not the same as in the device in this paper. Nonetheless, we can see that the coupling energy can be tuned from 0 to above 100 μeV.

For the coupling between qubit 1 and qubit 2, because tunneling is likely to occur when V_{U5} is not closed enough, we do not have many data points to systematically show the dependence of coupling energy J_{12} on V_{U5}.

When coupling strengths are strong enough, the conditioning of the target qubit's coherent oscillations becomes possible. To illustrate the mechanism of conditioning, we show in Fig. 7(e) typical experimental data of the Larmor

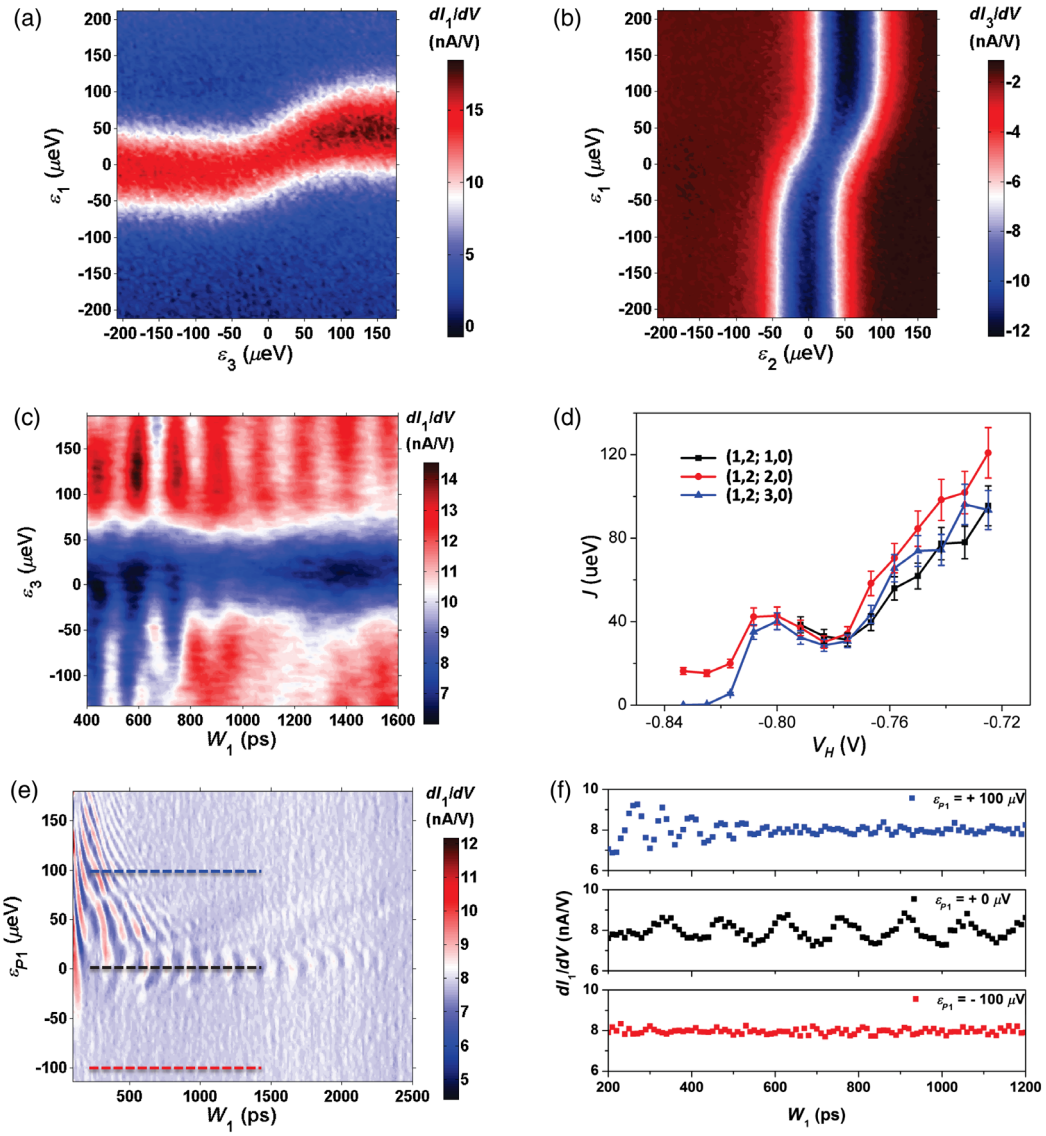

FIG. 7. (a),(b) When V_H is -0.85 V, the coupling between qubit 1 and qubit 3 J_{13} is measured to be about 50 μeV. (c) Tentative control experiment of qubit 1's coherent rotations by qubit 3 when V_H is -0.85 V. (d) Dependence of coupling energy J_{13} on V_H. (e) Larmor oscillations of qubit 1 dependent on the detuning energy that the adiabatic pulse drives the qubit to. (f) The top, central, and bottom panels compare the Larmor oscillations if the pulse drives the qubit above, to, and below the anticrossing point.

oscillations of the target qubit when it is decoupled from both control qubits. The x axis is the pulse width and the y axis is the detuning energy where the pulse drives the target qubit to denoted as ε_{P1}. Recorded is the differential current through QPC 1. We can see that the experimentally observed Larmor oscillations have a limited line width below the anticrossing point ($\varepsilon_{P1} < 0$) and have much broader decaying tails above the anticrossing point ($\varepsilon_{P1} > 0$).

In the central panel of Fig. 7(f), the black dots are a typical curve of Larmor oscillations when the pulse drives the qubit to the anticrossing point ($\varepsilon_{P1} = 0$). In the top panel, the blue dots show residual Larmor oscillations if the pulse drives the qubit above the anticrossing point by an amount about the same as $J(\varepsilon_{P1} = -100\ \mu\text{eV})$. Because the qubit coherence time is lower when detuning is off the anticrossing point, the Larmor oscillations dephase much faster. However, we still see residual oscillations, meaning that the enhanced dephasing effect alone does not completely suppress Larmor oscillations.

On the bottom panel, the red dots show that the Larmor oscillations are basically gone if the pulse drives the qubit below the anticrossing point ($\varepsilon_{P1} = -100\ \mu\text{eV}$). This is because Larmor precession reaches the maximum at the anticrossing point and deteriorates quickly with respect to the detuning for this two-level quantum system. Below the anticrossing point, Larmor precession has a small line width. If the pulse drives the qubit below the anticrossing point by an amount larger than the line width, the Larmor oscillations will be completely suppressed.

In conclusion, when the target qubit is coupled to the control qubits, if the J-induced detuning is larger than a certain line width, the target qubit's Larmor oscillations will be completely suppressed.

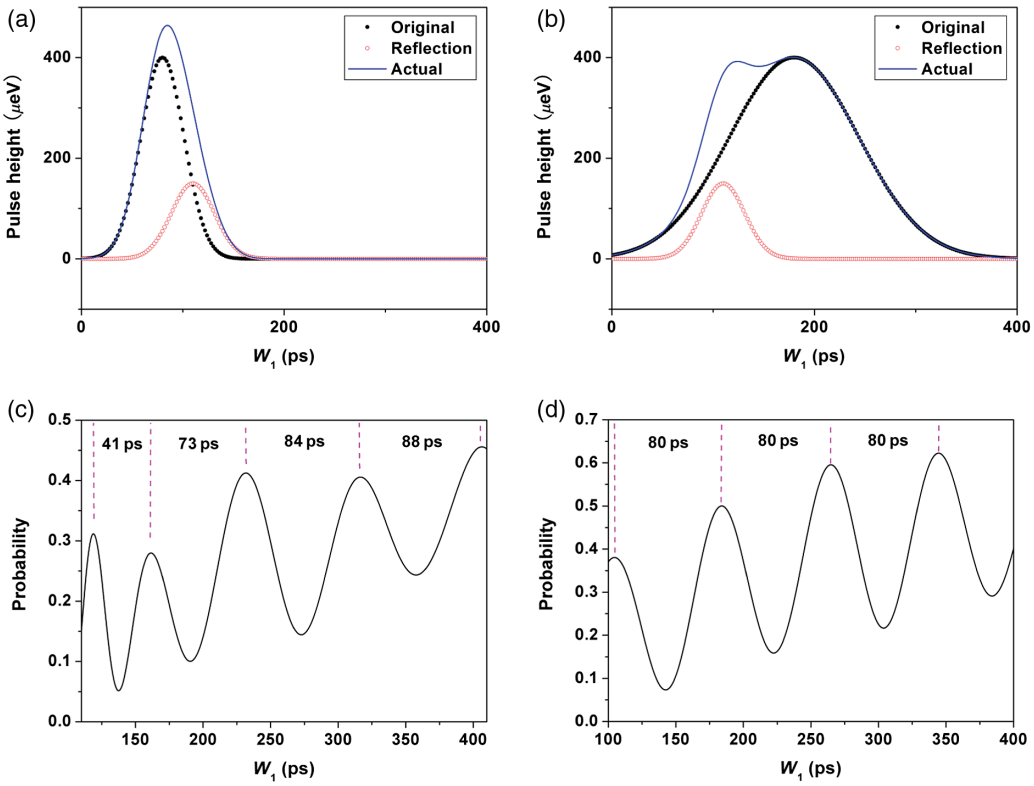

FIG. 8. (a),(b) Black closed dots are the original pulse. Red open circles are the reflection wave. Blue line is the actual pulse on the device gate. The original pulse width is 100 ps in (a) and 300 ps in (b). (c) Simulated LZS interference patterns after considering the pulse reflection. (d) Simulated LZS interference without pulse reflection.

APPENDIX D: PULSE IMPERFECTION AND ITS EFFECT

Because the qubit decoherence time in our experiment is approximately 1 ns, an ultrashort voltage pulse will be needed to operate all three qubits. This stringent requirement on pulse-shaping brings many technical challenges. For instance, the imperfections of pulse shape in the ultrashort pulse-width regime has some effects on our LZS interference patterns, as can be seen in Fig. 4 in the main text. In Fig. 4(a), we notice that the period of phase rotations is apparently shorter when the pulse width is ultrashort, that is, between 100 and 150 ps. We explain this nonperiodicity as pulse reflection.

When we apply high-frequency voltage pulses, there can be reflection on the circuit board where the device is mounted. The reflected wave comes back to the device and is superimposed on the original pulse. This modifies the pulse shape and gives rise to unexpected phenomena. In our example, we think the reflection pulse is superimposed on the peak of the original pulse and increases the pulse height when the original pulse is ultrashort (<150 ps). When the original pulse is wider (<150 ps), the reflection pulse is superimposed on the shoulder of the original pulse and mostly increases the pulse width. The period of LZS phase rotations decreases with pulse height and increases with pulse width. This is in agreement with the observed nonperiodicity in Fig. 4(a).

We simulate this effect and present the results in Fig. 8. We assume the reflection wave arrives at the device 30 ps later than the original pulse. The width of the reflection wave is assumed as 100 ps, and its amplitude is assumed to be one-third of the original pulse amplitude. Figure 8(a) shows that the pulse height is obviously increased when the original pulse width is 100 ps. Figure 8(b) shows that the pulse height almost does not change, and the pulse width essentially increases when the original pulse width is 300 ps.

As a result, nonperiodicity appears in the simulated LZS pattern, as shown in Fig. 8(c). The spacing between the first two peaks is 41 ps, significantly smaller than the following peak spacing, which is from 73 to 88 ps in this figure. In contrast, the simulated LZS interference without pulse reflection shows nearly perfect periodicity (80 ps) when the pulse width is from 100 to 400 ps, as presented in Fig. 8(d).

[1] J. R. Petta, A. C. Johnson, J. M. Taylor, E. A. Laird, A. Yacoby, M. D. Lukin, C. M. Marcus, M. P. Hanson, and A. C. Gossard, Coherent manipulation of coupled electron spins in semiconductor quantum dots, Science **309**, 2180 (2005).

[2] H. L. Koppens, C. Buizert, K. J. Tielrooij, I. T. Vink, K. C. Nowack, T. Meunier, L. P. Kouwenhoven, and L. M. K. Vandersypen, Driven coherent oscillations of a single electron spin in a quantum dot, Nature (London) **442**, 766 (2006).

[3] B. M. Maune, M. G. Borselli, B. Huang, T. D. Ladd, P. W. Deelman, K. S. Holabird, A. A. Kiselev, I. Alvarado-Rodriguez, R. S. Ross, A. E. Schmitz, M. Sokolich, C. A. Watson, M. F. Gyure, and A. T. Hunter, Coherent

singlet-triplet oscillations in a silicon-based double quantum dot, Nature (London) **481**, 344 (2012).

[4] E. Kawakami, P. Scarlino, D. R. Ward, F. R. Braakman, D. E. Savage, M. G. Lagally, Mark Friesen, S. N. Coppersmith, M. A. Eriksson, and L. M. K. Vandersypen, Electrical control of a long-lived spin qubit in a Si/SiGe quantum dot, Nat. Nanotechnol. **9**, 666 (2014).

[5] X. Wu, D. R. Warda, J. R. Pranceb, Dohun Kima, John King Gamblea, R. T. Mohra, Zhan Shia, D. E. Savagec, M. G. Lagallyc, Mark Friesena, S. N. Coppersmitha, and M. A. Eriksson, Two-axis control of a singlet–triplet qubit with an integrated micromagnet, Proc. Natl. Acad. Sci. U.S.A. **111**, 11938 (2014).

[6] M. Veldhorst, J. C. C. Hwang, C. H. Yang, A. W. Leenstra, B. de Ronde, J. P. Dehollain, J. T. Muhonen, F. E. Hudson, K. M. Itoh, A. Morello, and A. S. Dzurak, An addressable quantum dot qubit with fault-tolerant control-fidelity, Nat. Nanotechnol. **9**, 981 (2014).

[7] T. Hayashi, T. Fujisawa, H. D. Cheong, Y. H. Jeong, and Y. Hirayama, Coherent Manipulation of Electronic States in a Double Quantum Dot, Phys. Rev. Lett. **91**, 226804 (2003).

[8] K. D. Petersson, J. R. Petta, H. Lu, and A. C. Gossard, Quantum Coherence in a One-Electron Semiconductor Charge Qubit, Phys. Rev. Lett. **105**, 246804 (2010).

[9] G. Cao, Hai-Ou Li, Tao Tu, Li Wang, Cheng Zhou, Ming Xiao, Guang-Can Guo, Hong-Wen Jiang, and Guo-Ping Guo, Ultrafast universal quantum control of a quantum-dot charge qubit using Landau-Zener-Stuckelberg interference, Nat. Commun. **4**, 1401 (2013).

[10] D. Kim, D. R. Ward, C. B. Simmons, John King Gamble, Robin Blume-Kohout, Erik Nielsen, D. E. Savage, M. G. Lagally, Mark Friesen, S. N. Coppersmith, and M. A. Eriksson, Microwave-driven coherent operation of a semiconductor quantum dot charge qubit, Nat. Nanotechnol. **10**, 243 (2015).

[11] D. Kim, Zhan Shi, C. B. Simmons, D. R. Ward, J. R. Prance, Teck Seng Koh, John King Gamble, D. E. Savage, M. G. Lagally, Mark Friesen, S. N. Coppersmith, and Mark A. Eriksson, Quantum control and process tomography of a semiconductor quantum dot hybrid qubit, Nature (London) **511**, 70 (2014).

[12] G. Cao, Hai-Ou Li, Guo-Dong Yu, Bao-Chuan Wang, Bao-Bao Chen, Xiang-Xiang Song, Ming Xiao, Guang-Can Guo, Hong-Wen Jiang, Xuedong Hu, and Guo-Ping Guo, Tunable Hybrid Qubit in a GaAs Double Quantum Dot, Phys. Rev. Lett. **116**, 086801 (2016).

[13] R. Brunner, Y.-S. Shin, T. Obata, M. Pioro-Ladrière, T. Kubo, K. Yoshida, T. Taniyama, Y. Tokura, and S. Tarucha, Two-Qubit Gate of Combined Single-Spin Rotation and Interdot Spin Exchange in a Double Quantum Dot, Phys. Rev. Lett. **107**, 146801 (2011).

[14] K. C. Nowack, M. Shafiei, M. Laforest, G. E. D. K. Prawiroatmodjo, L. R. Schreiber, C. Reichl, W. Wegscheider, and L. M. K. Vandersypen, Single-shot correlations and two-qubit gate of solid-state spins, Science **333**, 1269 (2011).

[15] M. D. Shulman, O. E. Dial, S. P. Harvey, H. Bluhm, V. Umansky, and A. Yacoby, Demonstration of entanglement of electrostatically coupled singlet-triplet qubits, Science **336**, 202 (2012).

[16] M. Veldhorst, C. H. Yang, J. C. C. Hwang, W. Huang, J. P. Dehollain, J. T. Muhonen, S. Simmons, A. Laucht, F. E. Hudson, K. M. Itoh, A. Morello1, and A. S. Dzurak, A two-qubit logic gate in silicon, Nature (London) **526**, 410 (2015).

[17] G. Shinkai, Toshiaki Hayashi, Takeshi Ota, and Toshimasa Fujisawa, Correlated Coherent Oscillations in Coupled Semiconductor Charge Qubits, Phys. Rev. Lett. **103**, 056802 (2009).

[18] H. O. Li, Gang Cao, Guo-Dong Yu, Ming Xiao, Guang-Can Guo, Hong-Wen Jiang, and Guo-Ping Guo, Conditional rotation of two strongly coupled semiconductor charge qubits, Nat. Commun. **6**, 7681 (2015).

[19] D. M. Zajac, T. M. Hazard, X. Mi, E. Nielsen, and J. R. Petta, Scalable Gate Architecture for a One-Dimensional Array of Semiconductor Spin Qubits, Phys. Rev. Applied **6**, 054013 (2016).

[20] F. R. Braakman, P. Barthelemy, C. Reichl, W. Wegscheider, and L. M. K. Vandersypen, Long-distance coherent coupling in a quantum dot array, Nat. Nanotechnol. **8**, 432 (2013).

[21] A. Fedorov, L. Steffen, M. Baur, M. P. da Silva, and A. Wallraff, Implementation of a Toffoli gate with superconducting circuits, Nature (London) **481**, 170 (2013).

[22] M. Neeley, Radoslaw C. Bialczak, M. Lenander, E. Lucero, Matteo Mariantoni, A. D. O'Connell, D. Sank, H. Wang, M. Weides, J. Wenner, Y. Yin, T. Yamamoto, A. N. Cleland, and John M. Martinis, Generation of three-qubit entangled states using superconducting phase qubits, Nature (London) **467**, 570 (2010).

[23] L. DiCarlo, M. D. Reed, L. Sun, B. R. Johnson, J. M. Chow, J. M. Gambetta, L. Frunzio, S. M. Girvin, M. H. Devoret, and R. J. Schoelkopf, Preparation and measurement of three-qubit entanglement in a superconducting circuit, Nature (London) **467**, 574 (2010).

[24] Please see Appendix A for more details on the charge-sensing technique.

[25] K. D. Petersson, C. G. Smith, D. Anderson, P. Atkinson, G. A. C. Jones, and D. A. Ritchie, Microwave-Driven Transitions in Two Coupled Semiconductor Charge Qubits, Phys. Rev. Lett. **103**, 016805 (2009).

[26] Please see Appendix B for more information about the voltage-energy conversion scheme.

[27] G. D. Yu, Hai-Ou Li, Gang Cao, Ming Xiao, Hong-Wen Jiang, and Guo-Ping Guo, Tunable capacitive coupling between two semiconductor charge qubits, Nanotechnology **27**, 324003 (2016).

[28] Appendix C provides more details of the tuning of coupling strength and its effect on controlled coherent rotations.

[29] T. Fujisawa, Gou Shinkai, Toshiaki Hayashi, and Takeshi Ota, Multiple two-qubit operations for a coupled semiconductor charge qubit, Physica (Amsterdam) **43E**, 730 (2011).

[30] J. R. Petta, A. C. Johnson, C. M. Marcus, M. P. Hanson, and A. C. Gossard, Manipulation of a Single Charge in a Double Quantum Dot, Phys. Rev. Lett. **93**, 186802 (2004).

[31] G. Cao, Hai-Ou Li, Xiang-Xiang Song, Guo-Dong Yu, Bao-Bao Chen, Ming Xiao, and Guo-Ping Guo, Arbitrary phase

shift of a semiconductor quantum dot charge qubit on a short time scale, Europhys. Lett. **112**, 37005 (2015).

[32] Appendix D provides further discussion of the pulse imperfection.

[33] R. N. Shang, Hai-Ou Li, Gang Cao, Ming Xiao, Tao Tu, Hongwen Jiang, Guang-Can Guo, and Guo-Ping Guo, Photon-assisted-tunneling in a coupled double quantum dot under high microwave excitation powers, Appl. Phys. Lett. **103**, 162109 (2013).

[34] R. N. Shang, Li Hai-Ou, Cao Gang, Yu Guo-Dong, Xiao Ming, Tu Tao, and Guo Guo-Ping, Probing energy spectrum of quadruple quantum dots with microwave field, Chin. Phys. Lett. **31**, 050302 (2014).